

# Continuum limit of the adaptive Kuramoto model

Rok Cestnik<sup>1, a)</sup> and Erik A. Martens<sup>1</sup>

Centre for Mathematical Science, Lund University, Sölvegatan 18, 22100, Lund, Sweden

(\*Electronic mail: erik.martens@math.lth.se)

(\*Electronic mail: rok.cestnik@math.lth.se)

(Dated: 8 July 2024)

We investigate the dynamics of the adaptive Kuramoto model in the continuum limit with slow adaptation. This model is distinguished by dense multistability, where multiple states coexist for the same system parameters. The underlying cause of this multistability is that some oscillators can lock at different phases or switch between locking and drifting depending on their initial conditions. We identify new states, such as two-cluster states. To simplify the analysis we introduce an approximate reduction of the model via row-averaging of the coupling matrix. We derive a self-consistency equation for the reduced model and present a stability diagram illustrating the effects of positive and negative adaptation. Our theoretical findings are validated through numerical simulations of a large finite system. Comparisons to previous work highlight the significant influence of adaptation on synchronization behavior.

**The synchronization of coupled oscillators is a fundamental phenomenon observed in many natural and technological systems, from heartbeats to power grids and neural networks. Traditional models like the Kuramoto model have helped us understand how synchronization emerges, but real-world systems often involve adaptive couplings that evolve in time in dependence of the dynamics occurring on the network nodes, i.e., the oscillators. The resulting dynamics on and of the network leads to *co-evolutionary network dynamics*, posing a mathematically challenging situation to analyze. Our study explores the adaptive Kuramoto model for a large number of oscillators (the continuum limit), focusing on how slow adaptation influences synchronization. We identify new states, such as two-cluster states, and introduce a simplified model to analyze large systems easier. Our findings reveal that adaptation significantly affects synchronization behavior, leading to multiple coexisting states for the same parameters and complex dynamics depending on initial conditions. These theoretical insights are supported by numerical simulations, providing a deeper understanding of the role of adaptation in synchronized systems.**

## I. INTRODUCTION

The synchronization of coupled oscillators is a fundamental phenomenon observed in various natural and technological systems<sup>1,2</sup>, such as heartbeats<sup>3</sup>, power grids<sup>4</sup>, neural networks<sup>5,6</sup> etc. Traditional models like the Kuramoto model have significantly advanced our understanding of how synchronization emerges. However, real-world systems often exhibit adaptive coupling, which can enhance synchronization and substantially broadens the scope of dynamic behaviors.

Adaptive networks, where coupling weights evolve based on the dynamics of the nodes, are prevalent in nature and

technology<sup>7,8</sup>. This adaptation can lead to complex behaviors not seen in static networks, necessitating further study. Systems like the vascular network<sup>9</sup>, the glymphatic system of the brain<sup>10</sup>, osteocyte networks<sup>11</sup>, social networks<sup>12</sup>, and particularly neural networks<sup>13</sup> demonstrate the importance of such adaptive mechanisms for their efficient functioning.

In this context, studying large systems is important, as many natural systems consist of a vast number of interacting components. By examining the continuum limit, where the number of oscillators approaches infinity, we can gain deeper insights into the emergent behaviors and fundamental properties of large networks, benefiting from the simplifications that this theoretical limit provides.

In this paper, we explore the dynamics of the adaptive Kuramoto model in the continuum limit with slow adaptation. Section II examines the full equations of a large finite system through numerical simulations, identifying basic stationary and non-stationary states. Sec. III introduces an approximate model that reduces the dimensionality by considering the dynamics of row-averages of the coupling matrix. The reduced model facilitates analysis and is computationally more cost effective to simulate for large systems – this is the model the subsequent analysis is based on. Sec. IV introduces the notion of locked and drifting oscillators which we use in the following Sec. V where a self-consistency equation for the order parameter is derived. Sec. VI analytically examines the transition to synchrony while Sec. VII presents a detailed stability diagram based on the analysis of the self-consistency equation. Sec. VIII compares the results of the self-consistency with numerical simulations of the finite system.

## II. MICROSCOPIC MODEL

We generalize the Kuramoto mode to include adaptive rules, where the system consists of  $N$  phases  $\varphi_i$  and  $N^2$  edge

<sup>a)</sup>Also at Centre for Mathematical Science, Lund University, Sölvegatan 18, 22100, Lund, Sweden

variables  $\kappa_{ij}$  evolving according to the following equations<sup>14</sup>

$$\dot{\varphi}_i = \omega_i + \frac{1}{N} \sum_{j=0}^N \kappa_{ij} \sin(\varphi_j - \varphi_i), \quad (1a)$$

$$\dot{\kappa}_{ij} = \varepsilon(1 + a \cos(\varphi_j - \varphi_i) - \kappa_{ij}). \quad (1b)$$

The concept behind this choice of the adaptation rule<sup>14</sup> is that as the adaptation parameter  $a$  goes to zero, all edges asymptotically go to 1 and the original Kuramoto model is recovered. Throughout this paper we focus on the continuum limit  $N \rightarrow \infty$  with slow adaptation  $\varepsilon \rightarrow 0$ .

### A. Numerical simulations

Through naive explorative simulations of (1) with finite  $N$  one observes three qualitatively different macroscopically-stationary states (Fig. 1):

1. **Incoherent state:** phases are scattered uniformly and most coupling weights are close to 1. This state occurs if the frequency distribution is wide enough.
2. **One phase cluster:** a significant portion of phases lock to the mean field and form a single coherent cluster, while the remaining phases drift and are uniformly distributed. The coupling connecting two coherent oscillators have a larger weight  $\kappa_{ij} \approx 1 + a$  while remaining coupling weights are close to 1. This state occurs for a narrow enough frequency distribution.
3. **Two phase clusters:** two coherent phase clusters form, a main cluster and a smaller cluster at the antipodal phase. The coupling connecting oscillators of the same clusters again have large weight  $\kappa_{ij} \approx 1 + a$ , while coupling connecting two oscillators from the opposing clusters have negative weight  $\kappa_{ij} \approx 1 - a$ . All other coupling weights are close to 1. This state occurs for a narrow enough frequency distribution, large enough adaptivity  $a$  and particular initial conditions of both phases  $\varphi_i$  and couplings  $\kappa_{ij}$  (for incoherent initial conditions it is unlikely to reach 2-phase-cluster states).

See Fig. 1(a,b,c) for the depiction of these states, realized with a finite ensemble simulation  $N = 300$  and  $\varepsilon = 0.1$ . In the limit  $N \rightarrow \infty$ , provided the frequency distribution has infinite support, there is always a portion of oscillators whose phases do not lock to the mean field and so all observed quasi-stationary states feature aspects of partial synchrony<sup>15–17</sup>. However, if the frequency domain has a compact support (which is always the case in numerical realizations) one can also get fully locked states.

For negative adaptivity  $a < 0$  we also observe macroscopically non-stationary states, both periodic as well as chaotic, where the mean field changes both direction and amplitude in time, see Fig. 1(d). These states are reminiscent to those of recurrent synchronization<sup>18</sup> (periodic) and recurrent chaotic synchronization<sup>19</sup> (chaotic) which have recently been reported for finite sized adaptive systems.

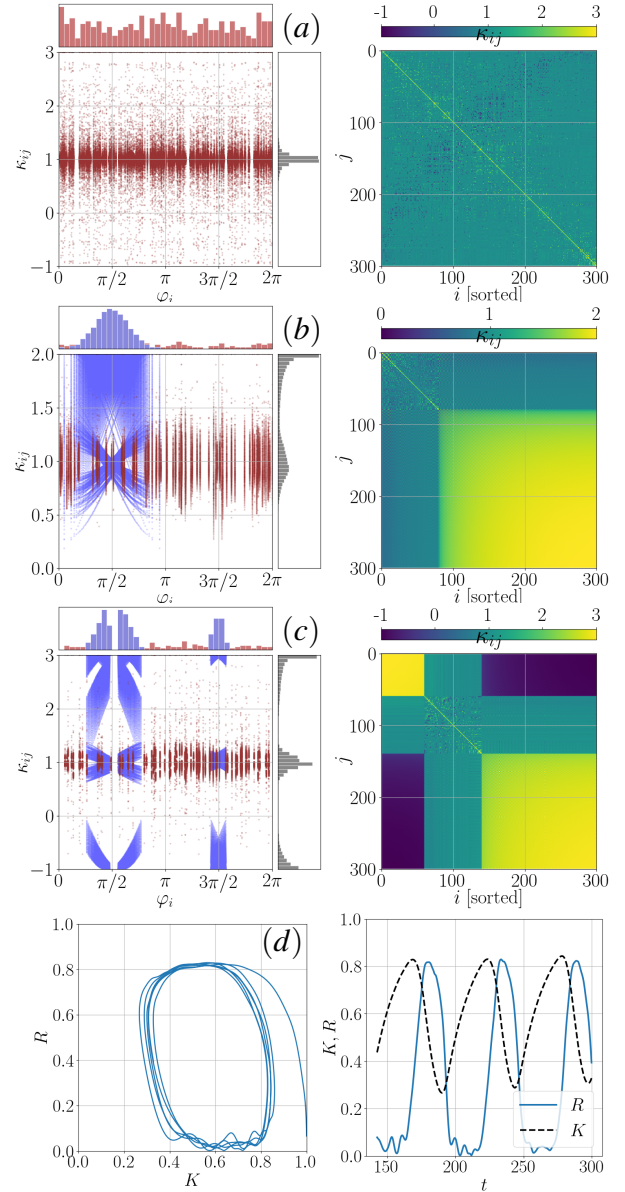


FIG. 1. (a-c) macroscopically stationary states observed by numerical simulation of Eqs. (1) using  $N = 300$  and  $\varepsilon = 0.1$ . In the left panels blue are phase-locked oscillators, red a drifters. In the right panels the coupling matrices are sorted with the average edge weights to reveal the phase clusters. (d) macroscopically periodic (possibly chaotic) state.  $R$  and  $K$  are the order parameters of phases and coupling strengths respectively:  $R = \left| \frac{1}{N} \sum_i e^{i\varphi_i} \right|$ ,  $K = \frac{1}{N^2} \sum_{i,j} \kappa_{ij}$ . Panel specific parameters are (a):  $(\sigma, a) = (2, 2)$ ; (b):  $(\sigma, a) = (1, 1)$ ; (c):  $(\sigma, a) = (1, 2)$ ; (d):  $(\sigma, a) = (0.5, -2)$ .

### III. ROW-AVERAGE APPROXIMATION

In system (1) the number of edges grows quadratically with the number of nodes which makes numerical simulations of large ensembles prohibitively slow. This is why, particularly when aiming at studying the system in the continuum limit  $N \rightarrow \infty$ , it is useful to consider simplifications. One such

simplification was done in Ref<sup>20</sup> where all edge weights are averaged and represented with a single macroscopic variable. However, here we desire to pursue a less drastic reduction, while preserving the information about the internal edge dynamics of the network, and instead treat the network topology as a nodal property. Specifically, we consider the row-average of the coupling matrix,

$$\kappa_i = \frac{1}{N} \sum_{j=0}^N \kappa_{ij}. \quad (2)$$

Constraining the dynamics of system (1) onto  $\kappa_i$  variables we obtain the following dynamical equations:

$$\dot{\phi}_i = \omega_i + \kappa_i R \sin(\Phi - \phi_i), \quad (3a)$$

$$\dot{\kappa}_i = \varepsilon(1 + aR \cos(\Phi - \phi_i) - \kappa_i), \quad (3b)$$

where  $R$  and  $\Phi$  are the phase order parameters:

$$R e^{i\Phi} = \frac{1}{N} \sum_{i=1}^N e^{i\phi_i}. \quad (4)$$

We can move into the rotation frame of reference and without loss of generality set  $\Phi = 0$ :

$$\dot{\phi}_i = \omega_i - \kappa_i R \sin(\phi_i), \quad (5a)$$

$$\dot{\kappa}_i = \varepsilon(1 + aR \cos(\phi_i) - \kappa_i). \quad (5b)$$

These are the equations we will analyze in this paper.

#### IV. LOCKED AND DRIFTING OSCILLATORS

We aim at analyzing the stationary partial synchrony states observed in Section II with a self-consistency equation. We follow Kuramoto<sup>15</sup> and Strogatz<sup>16</sup> in the derivation (see Section 4 of Ref.<sup>16</sup>). As an overview, we will evaluate the order parameter  $R$  via the integral:

$$R = \left| \int_{-\infty}^{\infty} g(\omega) \int_0^{2\pi} e^{i\phi} P(\phi, \omega) d\phi d\omega \right|, \quad (6)$$

where  $g(\omega)$  is the frequency distribution and  $P(\phi, \omega)$  is the probability density of oscillators at phase  $\phi$  and frequency  $\omega$ .

We split the oscillator population into two groups:

1. Phase-locked oscillators, denoted **locked**:  $\dot{\phi}_i = 0$ .
2. Phase-drifting oscillators, denoted **drifters**:  $\dot{\phi}_i \neq 0$ .

Note that for all asymptotically stable stationary states each oscillator can only either be locked or drifting. However, for  $a \neq 0$  there is always a range of natural frequencies that allow oscillators to be either locked or drifting depending on initial conditions, and both oscillator states provide a multitude of locally stable configurations with varying ratio of locked versus drifting oscillators (see green region in Fig. 2). Thus, the adaptive capability of the modified Kuramoto model in (5) allows for a high level of multistability that is absent for the

non-adaptive model. To make progress in terms of our analysis, we restrict our focus only to configurations with (i) symmetric phase oscillator distribution (i.e.,  $P(\phi) = P(-\phi)$  with  $P$  the (quasi-stationary) probability density distribution), and (ii) with maximal locking, i.e., the maximal amount of oscillators reside in the locked oscillator state – in other words, we adhere to the principle that "*all that can lock, do lock*". We denote the maximal possible frequency of locking with  $\omega_{\text{thr}}$ . For a discussion of challenges encountered for asymmetric distributions see Appendix C.

We may express the order parameter  $R$  as having two contributions – due to locked oscillators and drifters:

$$R = R_{\text{DRIFT}} + R_{\text{LOCK}} = \left| \int_{|\omega| > \omega_{\text{thr}}} \cdot d\omega \right| + \left| \int_{|\omega| < \omega_{\text{thr}}} \cdot d\omega \right|. \quad (7)$$

Let us first consider the **drifters**, the oscillators that do not lock to the mean field and for which  $\dot{\phi}_i \neq 0$ . Note that we anticipate a nearly identical calculation as in the case of the classical Kuramoto system<sup>15,16</sup>. Taking the limit  $\varepsilon \rightarrow 0$  we can average the fast phase dynamics in Eq. (5b)<sup>21,22</sup>:

$$\dot{\kappa}_i = \varepsilon(1 + aR \langle \cos(\phi_i) \rangle_t - \kappa_i), \quad (8)$$

where by  $\langle \cdot \rangle_t$  we denote the time average limit:  $\langle \cdot \rangle_t = \lim_{T \rightarrow \infty} \frac{1}{T} \int_0^T \cdot dt$ . In this averaged slow dynamics the  $\kappa_i$  tend towards a certain *stationary* value,

$$\kappa_i^{\text{st}} = 1 + aR \langle \cos(\phi_i) \rangle_t, \quad (9)$$

which means we can substitute this value into the phase equation (5a) and obtain a simple ensemble of phase oscillators coupled via the first harmonic, in similarity to the analysis for the Kuramoto model with heterogeneous coupling strengths<sup>16</sup>:

$$\dot{\phi}_i = \omega_i - (1 + aR \langle \cos(\phi_i) \rangle_t) R \sin(\phi_i). \quad (10)$$

Since we are considering drifting oscillators, we do not expect their phases to become stationary, but in the continuum limit of  $N \rightarrow \infty$  we do expect their probability density to be stationary. Their density is inversely proportional to their velocity:

$$P(\phi, \omega) = \frac{C}{|\dot{\phi}|} = \frac{C}{|\omega - (1 + aR \langle \cos(\phi) \rangle_t) R \sin(\phi)|}, \quad (11)$$

(with  $C \in \mathbb{R}$  the normalization constant). The term  $\langle \cos(\phi) \rangle_t$  turns out to be zero which implies  $\kappa_i^{\text{st}} = 1$ , and so for drifters the governing phase-equations are identical to the Kuramoto model (see Appendix A 1 for a derivation)<sup>23</sup>.

We can evaluate the integral (6) for drifters using the expression for their probability density (11). Importantly, keep notice of the symmetry:

$$P(\phi + \pi, -\omega) = P(\phi, \omega). \quad (12)$$

Also, we will only consider symmetric frequency distributions  $g(\omega) = g(-\omega)$ . Considering the symmetries of the phase density  $P(\phi, \omega)$  and frequency distribution  $g(\omega)$  we observe that

the integral for drifting oscillators vanishes, see Appendix A for the derivation. Thus, drifters do not contribute to the mean field  $R$  and we may ignore the  $R_{\text{DRIFT}}$  term<sup>24</sup>.

Now let us consider the **locked** oscillators, for which  $\dot{\varphi}_i = 0$ . Since their phases are locked, their probability density is effectively a  $\delta$  function in phase:  $P(\varphi, \omega) \propto \delta(\varphi^{\text{st}}(\omega))$ . This means the phase integral in (6) can be evaluated at the stationary phase  $\varphi^{\text{st}}(\omega)$  and only the frequency integration remains. We will now express this stationary phase value  $\varphi^{\text{st}}(\omega)$ .

Locked phases inevitably imply that the corresponding topology variable  $\kappa_i$  is also locked,  $\dot{\kappa}_i = 0$ . We can express the stationary value:

$$\kappa_i^{\text{st}} = 1 + aR \cos(\varphi_i). \quad (13)$$

(Note that we could also obtain this result by evaluating the time-averaged solution (9)). Substituting (13) into the fixed point condition for the phase equations (5a) yields the relation between phases  $\varphi_i$  and their corresponding frequencies  $\omega_i$ :

$$\omega = R \sin(\varphi) + \frac{aR^2}{2} \sin(2\varphi). \quad (14)$$

Note that (14) defines functional relation for each oscillator  $i$ ,  $\omega_i = f(\varphi_i)$ , which is not necessarily injective, i.e., for the same frequency  $\omega$  there can be more than one phase value  $\varphi$ . This is what gives rise to two phase cluster states, as we will see further below in the subsequent analysis. In Fig. 2 we plot relation (14) for different adaptivity  $a$ . There are three qualitatively different situations:

- $|a| < 1$ : (14) is injective, and the analysis is analogous to the regular Kuramoto model. Only 1-phase-cluster states are possible, see Fig. 2(a).
- $a > 1$ : (14) produces another bump around phase  $\pi$ , which can give rise to 2-phase-cluster antipodal states (main cluster around phase 0, and a smaller cluster around phase  $\pi$ ), see Fig. 2(b).
- $a < -1$ : (14) produces another bump around phase 0 which can give rise to (potentially unstable) 2-phase-cluster states (both clusters of roughly equal size on either side of phase 0), see Fig. 2(c).

The threshold values that determine phase locking regions  $\varphi_{\text{thr1}}$ ,  $\varphi_{\text{thr2}}$  can be expressed explicitly:

$$\varphi_{\text{thr1}} = \arccos\left(\frac{1}{4aR}\left(-1 + \sqrt{1 + 8a^2R^2}\right)\right), \quad (15a)$$

$$\varphi_{\text{thr2}} = \arccos\left(\frac{1}{4aR}\left(-1 - \sqrt{1 + 8a^2R^2}\right)\right), \quad (15b)$$

and so can the maximal locking frequency threshold:

$$\omega_{\text{thr}} = \omega(\varphi_{\text{thr1}}) = R\sqrt{\frac{(3 + \sqrt{1 + 8a^2R^2})^3}{32(1 + \sqrt{1 + 8a^2R^2})}}. \quad (16)$$

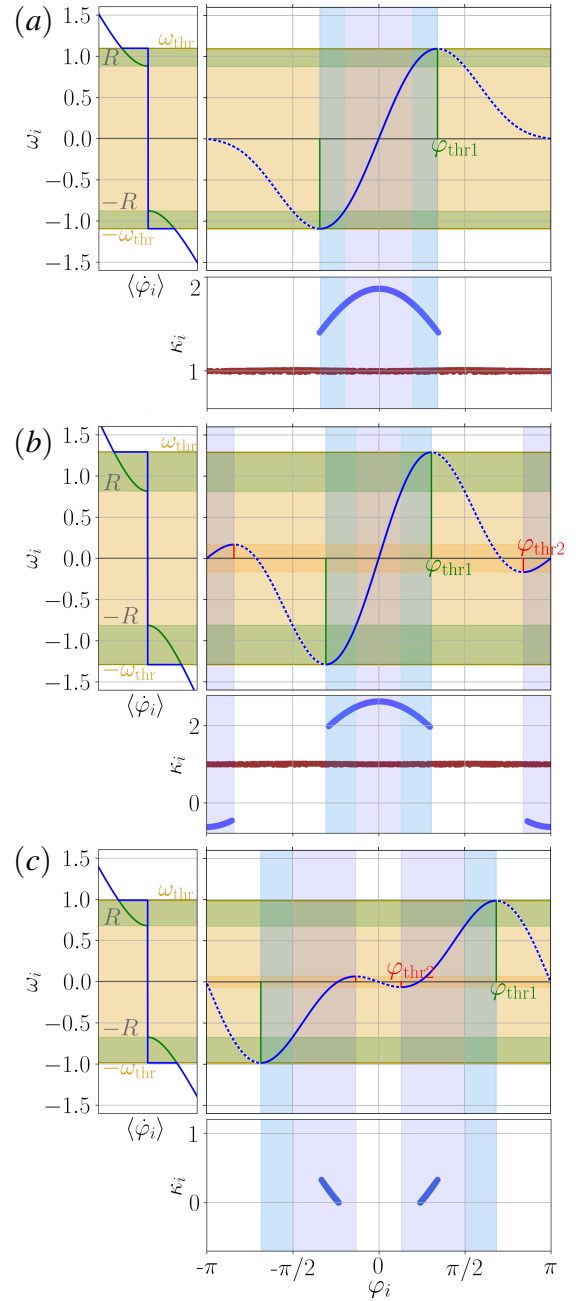


FIG. 2. The phase-frequency relation (14) in three qualitatively different situations. (a) injective relation with stable phases only around 0, parameters  $(a, R, \sigma) = (1, 0.88, 0.6)$ , (b) positive adaptation non-injectivity with additional stable phases around phase  $\pi$ , parameters  $(a, R, \sigma) = (2, 0.81, 0.65)$ , (c) negative adaptation non-injectivity, splitting of stable phases on either side of phase 0, parameters  $(a, R, \sigma) = (-2, 0.68, 0.05)$ . Each of the three panels additionally shows the effective frequency on the left, and an example state of system (5) on the bottom with  $\varepsilon = 0.01$  and  $N = 10^4$  (locked oscillators are blue, drifters are red). The shaded vertical/horizontal stripes mark particular phase/frequency domains: blue/orange marks the domain where oscillators lock and cyan/green marks the domain where oscillators can either drift or lock. The horizontal dark orange marks the frequency domain that allows locking at two distinct phases. Outside these regions oscillators drift. All illustrated states have configurations with maximum locking, obtained by using initial conditions with high absolute values for  $\kappa_i$ . The state of panel (c) has no drifters, corresponding to a fully locked state (due to finite  $N$ , note that the continuum limit always displays drifters).

## V. SELF-CONSISTENCY EQUATION FOR THE ORDER PARAMETER $R$

We define the order parameter  $R$  as the absolute value of the mean phase exponentials, i.e., Eq. (6). We have already seen that the drifters do not contribute to the order parameter and that the locked oscillators may only have 1 (or 2) phase values for each frequency  $\omega^{25}$ . We can therefore express the order parameter with an integral over the frequency only:

$$R = \left| \int_{-\omega_{\text{thr}}}^{\omega_{\text{thr}}} e^{i\varphi(\omega)} g(\omega) d\omega \right|. \quad (17)$$

Additionally, since we only consider symmetric phase distributions (with symmetric frequency distribution  $g(\omega)$ ) and move into the rotating frame of reference, we need only consider the real component of the order parameter (the integral over  $\sin(\varphi)$  cancels):

$$R = \int_{-\omega_{\text{thr}}}^{\omega_{\text{thr}}} \cos(\varphi(\omega)) g(\omega) d\omega. \quad (18)$$

However, it is worth noting that in general for non-symmetric phase distributions we have to consider the general case, see Appendix C for details.

We perform a change of variables using relation (14) and re-write the integral over the phases, while keeping in mind the non-injectivity of this relation. Thus we obtain a self-consistency equation for the order parameter  $R$ :

$$R = \int_{D(\varphi)} [R \cos^2(\varphi) + aR^2 \cos(\varphi) \cos(2\varphi)] \times g \left( R \sin(\varphi) + \frac{aR^2}{2} \sin(2\varphi) \right) d\varphi. \quad (19)$$

The phase domain  $D(\varphi)$  can be as simple as  $(-\varphi_{\text{thr1}}, \varphi_{\text{thr1}})$  but can also be non-trivial since we can have 2-phase cluster states (see blue region in Fig. 2). Also keep in mind that a portion of oscillators can either be locked or drifting depending on their initial conditions (green strip in Fig. 2), although we here always consider the maximal locking solution and thus "all that can lock, do lock".

### A. The choice of domain $D(\varphi)$

We have to be mindful of what we mean by integrating over the phases: we know that relation (14) is not necessarily injective, as well as some oscillators with natural frequencies  $R < |\omega| < \omega_{\text{thr}}$  may be locked or drifting. We also note that we have a choice in defining the integration domain  $D(\varphi)$ , as it corresponds to which states we are trying to capture with our self-consistency equation (19). For example, in the case of strong positive adaptation (Fig. 2(b)) we can consider only one cluster states and integrate only over the main branch around

$\varphi = 0$ ,

$$R = \int_{-\varphi_{\text{thr1}}}^{\varphi_{\text{thr1}}} \cdot d\varphi, \quad (20)$$

or we can consider a portion of oscillators to lock at a different phase and thus contribute to the second (antipodal) phase cluster. Only oscillators within a particular range of frequencies have this choice (see thin dark orange stripe in Fig. 2(b)). Specifically, suppose oscillators with frequencies ranging from  $-\omega^\dagger$  to  $\omega^\dagger$  go in the antipodal cluster. We can choose  $\omega^\dagger$  as the parameter. To write the integral in terms of the phase we then have to find the corresponding phase threshold values which we compute numerically by satisfying Eq. (14) with  $\omega^\dagger$  on the left-hand side. This yields two phase solutions, near zero:  $\varphi_0^\dagger$  and near  $\pi$ :  $\varphi_\pi^\dagger$ . The integral is then written as follows:

$$R = \int_{-\varphi_{\text{thr1}}}^{\varphi_{\text{thr1}}} \cdot d\varphi + \int_{\varphi_\pi^\dagger}^{2\pi - \varphi_\pi^\dagger} \cdot d\varphi - \int_{-\varphi_0^\dagger}^{\varphi_0^\dagger} \cdot d\varphi. \quad (21)$$

When we later perform the numerical quasi-continuation (Sec. VII) we slowly vary the  $\sigma$  parameter, and so for the branches we obtain the  $\omega^\dagger$  scales linearly:  $\omega^\dagger = c\sigma$ , where  $c \in \mathbb{R} > 0$  parametrizes different branches (see Fig. 3(b)).

For strongly negative adaptation we always get two phase-clusters (see Fig. 2(c)) but we still have to make a choice of the integration domain. We here only consider the symmetric solutions and an injective relation (14) where all negative frequencies go to one cluster and all positive to the other (this appears to be the common attractor for starting with a completely incoherent state). We have to look for the phase value that is the non-trivial zero of relation (14):  $\varphi^*$ , and the self-consistency integral is now written as:

$$R = \int_{-\varphi_{\text{thr1}}}^{-\varphi^*} \cdot d\varphi + \int_{\varphi^*}^{\varphi_{\text{thr1}}} \cdot d\varphi. \quad (22)$$

## VI. PHASE DIAGRAM

We analyze the row-averaged system (5) based on solving the self-consistency equation (19) using analytical (Section VI A) and numerical methods (Appendix B) to determine the associated stability diagram shown in Fig. 3. To examine non-stationary phase configurations, these results are further complemented by numerical simulations of Eq. (5) in Fig. 3(a).

### A. Incoherence-coherence transition

Looking at the self-consistency equation (19) we can see that, irrespective of parameter choice,  $R = 0$  is always a solution, corresponding to incoherent oscillations. The questions are whether this solution branch for the self-consistency

equation is the only one or if other solution branches exist, and if the branch  $R = 0$  describes a stable oscillator configuration. Following the steps of Kuramoto's original analysis<sup>16</sup>, we consider (19) in the limit  $R \rightarrow 0$  which yields

$$1 = g(0) \int_{D(\varphi)} \cos^2(\varphi) d\varphi, \quad (23)$$

for which the integration domain in this case is  $(-\pi/2, \pi/2)$ . Studying this reduced self-consistency equation, we may find a condition for which another solution arises. The integral in (23) evaluates to  $\pi/2$  so that the transition only depends on the shape of the frequency distribution, more specifically, the value of the frequency distribution at  $\omega = 0$ ,

$$g(0) = \frac{2}{\pi} \quad (24)$$

We consider a specific choice for  $g$ , the normal distribution,

$$g(x) = \frac{1}{\sigma} \frac{1}{\sqrt{2\pi}} \exp\left(-\frac{1}{2} \frac{x^2}{\sigma^2}\right), \quad (25)$$

in which case the critical value for the onset of a non-trivial solution branch of  $R$  is

$$\sigma_c = \sqrt{\frac{\pi}{8}} \approx 0.626657\dots \quad (26)$$

We indicate this critical  $\sigma_c$  as a black vertical line in Fig. 3(a). Furthermore, we ask what is the shape for small  $R$  near this transition point. Expanding (23) in terms of  $\sigma$ , we find that

$$R = \frac{1}{a} \frac{\sigma - \sigma_c}{C} + \mathcal{O}(\sigma^2), \quad (27)$$

where  $\sigma_c = \sqrt{\frac{\pi}{8}}$  and  $C = \int \cos(\varphi) \cos(2\varphi) d\varphi / \sqrt{2\pi} = \sqrt{\frac{2}{9\pi}}$ .

## B. Non-adaptive limit ( $a = 0$ ) and small adaptation ( $a \approx 0$ )

We continue by explaining the dynamics for the case of no adaptation, which is identical to the dynamics observed for the classical Kuramoto model. There are only two regions: the incoherent region where  $R = 0$ ; and a partially synchronous region where  $R > 0$ . The transition from incoherence to partial synchrony was analytically determined by Eq. (26), shown as a black line in Fig. 3 (b,c). The shape of the order parameter (gray curve in Fig. 3(b) and (c), Fig. 4(a) and (b)) near this transition is approximated by Eq. (27).

Any non-zero amount of adaptation allows some oscillators to reside in either locked or drifting configurations, consistent with a certain range of natural frequencies (see Section IV). Thus for non-zero adaptivity,  $a \neq 0$ , there always is a spectrum of neutrally stable configurations for the oscillators to occupy, corresponding to varying ratios of locked versus drifting oscillators that result in slightly different  $R$  values<sup>26</sup>. As mentioned previously (Section IV), we always focus on the maximal locking configurations (Fig. 3 depicts only branches with maximal locking).

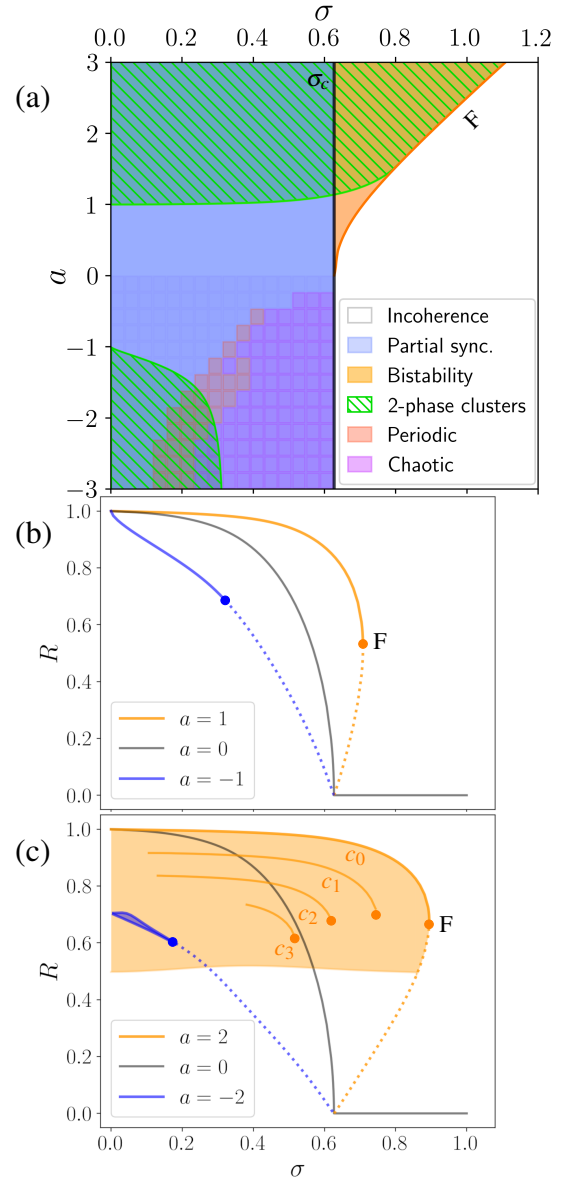


FIG. 3. (a) Phase diagram. The transition from the incoherent to the partial synchronous state at  $\sigma_c = \sqrt{\pi/8}$  (black line) is independent of adaptivity  $a$ . For positive adaptivity  $a > 0$  a fold bifurcation (orange curve F) is seen in the  $\sigma > \sigma_c$  region. A region of bi-stability (orange) between incoherence and partial synchrony lies between the fold bifurcation and transition at  $\sigma_c$ . 2-phase-cluster states with high level of multistability can occur in a parameter region (green hatching) characterized by a non-injective phase frequency relationship (14). For  $a > 0$  all states are stationary; more intricate dynamics are possible for  $a < 0$ : numerical integration of Eqs. (5) reveals stationary solutions (blue squares) for small  $\sigma$ ; periodic solutions (red) for larger  $\sigma$ ; and chaotic dynamics for even larger  $\sigma$  (purple). (b),(c) Order parameter  $R$  as function of  $\sigma$  by solving the self-consistency equation (19), and the classical Kuramoto transition (black) as comparison. (b) Intermediate adaptivity: Positive  $a = 1$  (orange curve) reveals a fold bifurcation (F), which is absent for negative adaptivity (blue curve for  $a = -1$ ). (c) Stronger adaptivity: For positive  $a = 2$  we observe a region of dense multistability: neutrally stable branches (orange curves) corresponding to non-trivial 2-phase-clusters with varying  $c$  values (see Section IV) are shown:  $c_0 = 0$ ,  $c_1 = 0.05$ ,  $c_2 = 0.1$ ,  $c_3 = 0.3$ . For negative  $a = -2$  the stationary branch is mostly unstable (dotted blue curve) with periodic/chaotic solutions. For small  $\sigma$  a narrow region with 2-phase-clusters is observed.



### C. Positive adaptation: bistability of synchrony/incoherence and 2-phase-cluster states

With positive adaptation, the domain of partial synchrony extends to the region with  $\sigma > \sigma_c$  until it disappears in a fold bifurcation (orange curve in Fig. 3(a)). In this region, configurations of partial synchrony and incoherence co-exist as stable states (orange region in Fig. 3(a)). When adaptivity  $a$  is raised above a critical value, we observe additional 2-phase cluster states (hatched green region in Fig. 3(a)). For each parameter choice where 2-phase clusters occur, they form a continuum of coexisting 2-phase-cluster states that occupy a range of different  $R$  values (shaded orange region in Fig. 3(c)). The full lines within the orange shaded regions in Fig. 3(c) represent specific choices for 2-phase-cluster state branches, obtained by solving the self-consistency equation (19). The hatched boundary in Fig. 3(a) was found by expressing the self-consistency equation in terms of  $a$  for the condition  $R = \frac{1}{a}$  and solving it, see Appendix B. Note that all states are macroscopically stationary partial synchrony states.

### D. Negative adaptation: 2-phase-cluster states and non-stationary states

With negative adaptation we do not observe any bistability regions between partially synchronous and incoherent states, since the asymptotic behavior of  $R$  around the critical point  $\sigma_c$  has a negative slope (see blue curve in Fig. 3(b)). At every negative  $a$  value there seems to be a range of  $\sigma$  that produce non-stationary oscillator states. To characterize these states we sampled parameter space on a grid by numerically simulating Eq. (5) with  $N = 10^4$  oscillator nodes. Thus, it was possible to determine whether or not observed states correspond to stationary, periodic or chaotic oscillator configurations (blue, red and purple grid cells in Fig. 3(a)). Furthermore, for strong negative adaptation, one may also observe 2-phase-cluster states (hatched green region in Fig. 3(a)); however, these state appear only to be stationary for a rather narrow frequency distributions. For these 2-phase-cluster states we also see a family of solution branches featuring a range of different  $R$  values (blue shaded region in Fig. 3(c)), but this variation is much less pronounced when compared to positive adaptivity  $a$  (orange shading).

## VII. VALIDATION OF SELF-CONSISTENCY WITH NUMERICAL SIMULATIONS

We compare our results obtained with the self-consistency equation (19) with direct simulations of the finite row-averaged system (5), using  $N = 10^4$  oscillators with a time scale separation of  $\varepsilon = 0.1$ . To do this, we numerically integrated Eq. (5) and performed a quasi-adiabatic continuation while varying the parameter  $\sigma$ . Results are shown in Fig. 4.

For positive adaptation, we consider  $a = 2$  and perform forward and backward quasi-continuation sweeps in  $\sigma$  (black circles in Fig. 4(a), starting from the incoherent state at  $\sigma = 1.1$

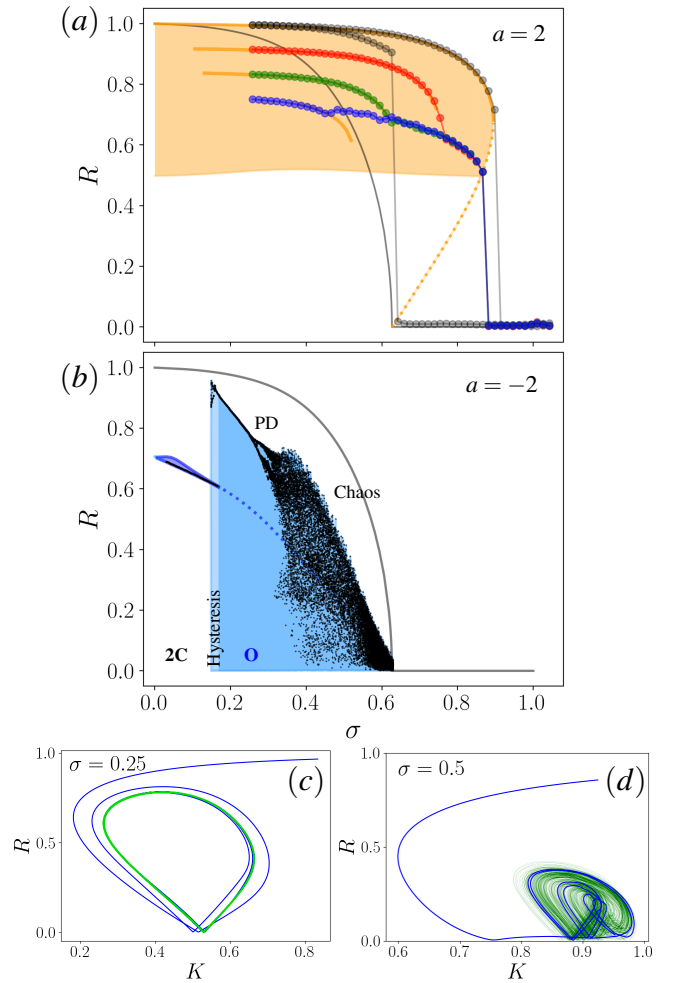


FIG. 4. (a),(b) Bifurcation diagrams obtained via quasi-continuation of the row-averaged model (5) with  $N = 10^4$  oscillators and  $\varepsilon = 0.1$ . (a) For positive adaptation,  $a = 2$ : several sweeps using different initial conditions (see text) reveal a family of neutrally stable solution branches (black, red, green, blue circles), matching well the solutions of the self-consistency equation with varying values of  $c$  (orange curves, same values as in Fig. 3(c)). Quasi-continuation in forward/backward direction reveals hysteresis (black circles). (b) Negative adaptation,  $a = -2$ : forward and backward continuation reporting  $\max_t R$  reveal stable stationary solutions (2C), and periodic solutions (O, blue shaded region) undergoing a cascade of period doubling bifurcations (PD) leading to chaotic dynamics (Chaos). A narrow region around  $\sigma = 0.16$  with bistability between stationary and non-stationary solutions is observed (Hysteresis). (c) Example trajectory of a periodic state with  $a = -2$ . (d) Example trajectory of a chaotic state with  $a = -2$ .

and decreasing  $\sigma$ . We observe that the transition from incoherence to partial synchrony occurs roughly at the critical value  $\sigma_c$ ; the order parameter jumps to a high value, but not to the maximally possible value – this is because it goes to a state of less than maximal locking, i.e., some oscillators that could lock remain drifting. As we continue to decrease  $\sigma$  the branch merges with the branch of maximal locking (top orange curve). Now we reverse the direction of  $\sigma$  continuation and see that the system follows the top stable branch of max-

imal locking and drops to incoherence at the fold bifurcation (F) as expected (see black points in Fig. 4(a)) – i.e., we observe a clear hysteresis loop.

We also performed three other sweeps (red, green and blue circles in Fig. 4(a)) starting from a narrow distribution at  $\sigma = 0.25$  with a 2-phase cluster initial condition with different sizes of the antipodal cluster<sup>27</sup>. The branches from numerical simulation follow the branches obtained from the self-consistency equation for the most part; but then suddenly collapse onto a certain branch they all share in common. Finally, this branch ceases to exist in a fold bifurcation and the incoherent state is obtained.

For negative adaptation, we consider  $a = -2$  and perform a sweep of the partially synchronous region in both directions, see Fig. 4(b) (starting at the critical  $\sigma_c$  with incoherent initial conditions). The region between the minimum and maximum value of the order parameter  $R$  is shaded blue. Stationary solutions occurring for small  $\sigma$  values are distinguished from the non-stationary solutions seen for larger  $\sigma$  values. We also plot the time-local maxima of the order parameter,  $\max_t(R)$ , to be able to distinguish periodic and chaotic solutions. Additionally, we notice a small hysteresis around  $\sigma \approx 0.16$  where there seems to be a co-existence of the stationary and non-stationary solutions. We expect that this bifurcation diagram depends on the specific choice of parameter  $\varepsilon$ .

## VIII. DISCUSSION

In this paper, we investigated the dynamics of the adaptive Kuramoto model in the continuum limit with slow adaptation. Key highlights include the identification of different states, including two-cluster states within dense regions of multistability, and the finding that some oscillators can either lock or drift depending on initial conditions. We introduced a reduced approximative model, simplifying the analysis for large systems. We derived a self-consistency equation for the order parameter, revealing the conditions for the transition to synchrony. We presented a stability diagram, highlighting the effects of positive and negative adaptivity, including regions of bistability and multistability for positive adaptivity, and non-stationary states for negative adaptivity. Finally, we validated our theoretical findings through numerical simulations, confirming the predicted behaviors and transitions.

The adaptive Kuramoto model we studied introduces significant differences compared to its classical non-adaptive counterpart. While the classical Kuramoto model produces only asymptotically stationary states (on the macroscopic scale) of either complete incoherence or partial synchrony, the adaptive model exhibits a richer variety of behaviors, including macroscopically non-stationary states (see Fig. 1(d) and Fig. 4(c,d)). Additionally the adaptive model shows dense multistability of states for the same parameters but different initial conditions. Notably, it can produce clear two-phase cluster states (Fig. 1(c), Fig. 2(b)) and generally asymmetric phase distributions, unlike the symmetric unimodal phase distributions observed in the classical model (for symmetric frequency distributions). This highlights the enhanced complex-

ity and dynamic richness of the adaptive Kuramoto model. Moreover, the high degree of multistability in the adaptive Kuramoto model suggests potential applications in memory tasks, as the system's ability to exist in numerous states can be harnessed to represent multiple memory configurations, thereby facilitating learning and information storage.

On the microscopic scale, the adaptive Kuramoto model also shows significant differences from the classical model. In the Kuramoto model, each phase can have either only one fixed point or no fixed points, which determines whether it locks or drifts respectively. However, in the adaptive model, there is a range of natural frequencies that allow oscillators to either drift or lock depending on their initial conditions (see Fig. 2). This ability to either drift or lock contributes to the multistability of states observed on the macroscopic scale.

We now compare our reduced row-averaged model (5) to the full  $N^2$  edge model (1). All discussed phenomena (non-stationarity, dense multistability and 2-phase cluster states) are present in both models. While it is possible that the full model exhibits additional phenomena not captured by the reduced version, we did not observe any and expect that all the interesting features one might find in the full model also appear in the reduction in some form. There are certainly quantitative differences between the two however. The two models are most similar under conditions of small adaptivity  $a$ , near incoherence ( $R \approx 0$ ), or near high synchrony ( $R \approx 1$ ) single cluster states. Settings where they differ most involve high adaptivity and pronounced 2-phase cluster states. For example, here we describe the most difference-contrasting setting we can think of:  $a \gg 1$  and a nearly 50-50 split 2-phase cluster state. In the full model, the main cluster at phase zero would have very high  $\kappa_i$  values, and the other cluster at phase  $\pi$  would have highly negative  $\kappa_i$  values. This state is very stable in the full model, with the first order parameter  $R$  close to zero and the second order parameter  $R_2 = \langle e^{i2\varphi} \rangle$  close to one. In the reduced model, such a state would not be as pronounced and might not be able to sustain such an even split due to  $R \approx 0$ .

The high dimensionality inherent to adaptive networks raises the question whether we can study reduced models instead, while appropriately capturing the complexity of the dynamics. It is therefore interesting to compare different methods of dimensional reduction. Our reduced row-averaged model (5) contrasts with the even more reduced model by Duchet *et al.*<sup>20</sup> (D2) in several ways. The reduction used in the work by Duchet *et al.* relies on averaging the coupling matrix to a single dynamic variable and combining this with Ott-Antonsen reduction applied to the phase dynamics<sup>28,29</sup>. Thus, both the coupling and phase dynamics are each reduced to single mean field variables. As such, the resulting approximated two dimensional dynamics of the single population Duchet model (Appendix D) cannot exhibit chaos; however, the model can exhibit macroscopically periodic states (see Appendix D). The macroscopic model only represents single cluster states and cannot display any microscopic effects such as oscillators having a choice of locking or drifting, nor can it represent the associated coupling strengths. Moreover, the Duchet model does not display non-stationary states



for  $a > -1$  (Appendix D); this stands in contrast to our larger dimensional model relying on row-averaging. This observation illustrates well the compromises one may pay for any type of approximate dimensional reduction. However, due to its simplicity one can consider a multi-population Duchet model, which assumes there are several populations of oscillators. The dynamics of each population is represented by its own order parameter, which interact via the multi-population coupling. To represent simple 2-phase-cluster states at least a two population model is required. The downside is that one has to choose the proportions of locked versus drifting oscillators in each population as a predetermined parameter (similar to choosing the value of  $c$  in (19)); By contrast, our row-averaged model settles into one of a family of phase (and coupling) configurations depending on initial conditions; an example are 2-phase-cluster states, where individual oscillators reside in one of two specific phase configurations (while at the same time, they can reside in drift versus locked phases, too). Thus, this proportion has the character of an emergent property.

We now compare the continuum limit to the previous work of only two adaptive oscillators<sup>14</sup>, highlighting the key similarities and differences. The adaptivity parameter  $a$  has the same role in both cases, but the width of the frequency distribution  $\sigma$  does not have a one-to-one analog in the 2 oscillator case, however we it can roughly relate to the frequency mismatch of the two oscillators. We focus on figures Fig. 3(a) and Fig. 3 in Ref.<sup>14</sup> as they offer the clearest comparison. We identify 3 points of comparison: (I) in both cases the domain of synchronization increases with adaptation. However, in the continuum model negative adaptation does not increase the synchrony domain, while in the two-oscillator case it still increases (though less than with positive adaptation). (II) in both cases there exist situations where the oscillators may either lock or drift depending on the initial conditions. However, in the continuum limit for any non-zero adaptation there is a portion of oscillators that can drift or lock, while for two oscillators there is only a specific parameter region that allows where this occurs. (III) In both cases there exists a parameter region which allows (some) oscillators to lock at 2 different phases, and in both cases those regions are for  $|a| > 1$ . In the continuum limit this allows for the 2-phase clusters, while for two oscillators it just means more possible stable solutions. These comparisons highlight the fundamental behavior observed in both systems and demonstrate the general influence of adaptation on phase oscillators, scaling from two oscillators to a continuum.

## ACKNOWLEDGMENTS

We wish to acknowledge C. Bick and F. Augustsson for helpful comments and discussions. We gratefully acknowledge financial support from the Royal Swedish Physiographic Society of Lund.

## AIP DATA SHARING POLICY

Data sharing is not applicable to this article as no new data were created or analyzed in this study.

## Appendix A: Contribution of drifters to the mean field $R$

Let us evaluate the integral (6) just for the drifters, using the expression for their probability density (11). Importantly, remember that we only consider symmetric frequency distributions  $g(\omega) = g(-\omega)$ , and the phase density symmetry:  $P(\varphi + \pi, -\omega) = P(\varphi, \omega)$ . Combining these two symmetries we can split the frequency integral in two intervals of  $\omega$ :

$$\int_{|\omega| > \omega_{\text{thr}}} g(\omega) \int_0^{2\pi} e^{i\varphi} P(\varphi, \omega) d\varphi d\omega = \int_{\omega < -\omega_{\text{thr}}} g(\omega) \int_0^{2\pi} e^{i\varphi} P(\varphi, \omega) d\varphi d\omega + \int_{\omega > \omega_{\text{thr}}} g(\omega) \int_0^{2\pi} e^{i\varphi} P(\varphi, \omega) d\varphi d\omega. \quad (\text{A1})$$

In the first integral apply a transformation of variables:  $\omega \mapsto -\omega$ :

$$\int_{\omega > \omega_{\text{thr}}} g(-\omega) \int_0^{2\pi} e^{i\varphi} P(\varphi, -\omega) d\varphi d\omega + \int_{\omega > \omega_{\text{thr}}} g(\omega) \int_0^{2\pi} e^{i\varphi} P(\varphi, \omega) d\varphi d\omega. \quad (\text{A2})$$

Using the symmetry of the frequency distribution,  $g(\omega) = g(-\omega)$ , we can combine both terms in a single integral:

$$\int_{\omega > \omega_{\text{thr}}} g(\omega) \int_0^{2\pi} e^{i\varphi} [P(\varphi, -\omega) + P(\varphi, \omega)] d\varphi d\omega. \quad (\text{A3})$$

Recalling the symmetry  $P(\varphi + \pi, -\omega) = P(\varphi, \omega)$ , we see that in terms of phase the two contributions (terms of  $P$ ) are simply shifted with respect to each other by a phase-shift of  $\pi$ ,

$$\int_0^{2\pi} e^{i\varphi} [P(\varphi - \pi, \omega) + P(\varphi, \omega)] d\varphi. \quad (\text{A4})$$

We split the integration intervals into two,

$$\int_0^{\pi} e^{i\varphi} [P(\varphi - \pi) + P(\varphi)] d\varphi + \int_{\pi}^{2\pi} e^{i\varphi} [P(\varphi - \pi) + P(\varphi)] d\varphi, \quad (\text{A5})$$

and with a transformation of variables:  $\varphi \mapsto \varphi - \pi$  in the second integral (and keeping in mind that  $P(\varphi)$  is  $2\pi$ -periodic) we see that the two integrals cancel each other:

$$0 = \int_0^{\pi} e^{i\varphi} [P(\varphi - \pi) + P(\varphi)] d\varphi - \int_0^{\pi} e^{i\varphi} [P(\varphi - 2\pi) + P(\varphi - \pi)] d\varphi. \quad (\text{A6})$$

Therefore, the net contribution of drifters to the mean field  $R$  is zero.

### 1. Evaluating stationary $\kappa_i$ -values for drifters

We can express the  $\kappa_i^{\text{st}}$  variables as:

$$\kappa_i^{\text{st}} = 1 + aR \langle \cos(\varphi_i) \rangle_t. \quad (\text{A7})$$

We attempt to compute the averaged term  $\langle \cos(\varphi) \rangle_t$ . We can rewrite the associated integral in terms of phase  $\varphi$  using the density (11),

$$\begin{aligned} \langle \cos(\varphi) \rangle_t &= \lim_{T \rightarrow \infty} \frac{1}{T} \int_0^T \cos(\varphi(t)) dt = \frac{1}{2\pi} \int_0^{2\pi} \cos(\varphi) P(\varphi, \omega) d\varphi = \\ &= \frac{C}{2\pi} \int_0^{2\pi} \frac{\cos(\varphi)}{|\omega - (1 + aR \langle \cos(\varphi) \rangle_t) R \sin(\varphi)|} d\varphi. \end{aligned} \quad (\text{A8})$$

Since the term  $\langle \cos(\varphi) \rangle_t$  is time-averaged it does not depend on phase  $\varphi$ , meaning that on the right we just have an integral

$$f(R) = \int_{-\varphi_{\text{thr1}}}^{\varphi_{\text{thr1}}} [R \cos^2(\varphi) + aR^2 \cos(\varphi) \cos(2\varphi)] g \left( R \sin(\varphi) + \frac{aR^2}{2} \sin(2\varphi) \right) d\varphi, \quad (\text{B1a})$$

$$R_{n+1} = f(R_n) \quad (\text{B1b})$$

which converges when using an initial guess  $0 \leq R_0 < 1$  and fixed  $\sigma$ . We may start this iteration scheme using a large  $0 < R < 1$  as initial value consistent with partial synchrony, as expected for small  $\sigma$ . Upon convergence, we may progressively increase  $\sigma$  and solve for the next value of  $R(\sigma)$ . This process is continued until we find values of  $\sigma$  with  $R \rightarrow 0$ , corresponding to incoherence.

We also know that for high  $|a|$  we get the intriguing 2-cluster states. The point at which these may occur is when the phase-frequency relationship (14) becomes non-injective, i.e., when

$$R = \frac{1}{|a|}. \quad (\text{B2})$$

$$f(a) = \left[ \int_{-\varphi_{\text{thr1}}}^{\varphi_{\text{thr1}}} \left[ \frac{1}{a} \cos^2(\varphi) + \frac{1}{a} \cos(\varphi) \cos(2\varphi) \right] g \left( \frac{1}{a} \sin(\varphi) + \frac{1}{2a} \sin(2\varphi) \right) d\varphi \right]^{-1}, \quad (\text{B4a})$$

$$a_{n+1} = f(a_n). \quad (\text{B4b})$$

### Appendix C: Self-consistent equation for the asymmetric phase distribution

In the main text we only consider symmetric phase distributions, but here we outline how the analysis would look like

of a trigonometric function over its period, and that equals to zero:  $\int_0^{2\pi} \frac{\cos(\varphi)}{\omega - A \sin(\varphi)} d\varphi = 0$ , ( $A \in \mathbb{R}$  just a constant). We can therefore conclude that the term  $\langle \cos(\varphi) \rangle_t$  must be zero,

$$\langle \cos(\varphi) \rangle_t = 0. \quad (\text{A9})$$

This result combined with (9) implies that the stationary value for the coupling strengths of drifters simply is given by

$$\kappa_i^{\text{st}} = 1. \quad (\text{A10})$$

As a consequence, this means that – considering drifters – the phase equation (10) now looks identical to that of the Kuramoto system<sup>15</sup>, and so the same analysis<sup>16</sup> applies here.

### Appendix B: Iterative solution of the self-consistency equation

The fold of the transition for positive  $a$  (red line in Fig. 3) is solved numerically by iteratively solving the self-consistency equation (19):

With this condition, we may rewrite the iterative scheme for solving the corresponding self-consistency condition in terms of  $a$  only. Thus, we may compute the boundaries of existence for the 2-cluster states (blue lines in Fig. 3). First we evaluate the integration boundaries  $\varphi_{\text{thr1}}$  (15a):

$$\varphi_{\text{thr1}} = \begin{cases} \frac{\pi}{3} & \text{for } R = \frac{1}{a} \\ \frac{2\pi}{3} & \text{for } R = -\frac{1}{a} \end{cases} \quad (\text{B3})$$

Then we obtain the following iteration scheme:

for the case of states with asymmetric phase distributions. We

can still move into the co-rotating frame of reference  $\Phi = 0$  and still get stationary coupling:  $\kappa_i^{\text{st}} = 1 + aR \cos(\varphi_i)$ . But the ensemble-averaged dynamic frequency  $\langle \dot{\varphi}_i \rangle$  may differ from the mean frequency  $\langle \omega_i \rangle$ , and is expressed as:

$$\langle \dot{\varphi}_i \rangle = -R \langle \sin(\varphi_i) \rangle - \frac{aR^2}{2} \langle \sin(2\varphi_i) \rangle, \quad (\text{C1})$$

(we here denote the ensemble average with  $\langle \cdot \rangle = \frac{1}{N} \sum_i \cdot$ ). The locked oscillators still all have identical frequency:  $\dot{\varphi}_i = \langle \dot{\varphi}_i \rangle$

which we use to express the phase-frequency relation:

$$\omega_i = R [\sin(\varphi_i) - \langle \sin(\varphi_i) \rangle] + \frac{aR^2}{2} [\sin(2\varphi_i) - \langle \sin(2\varphi_i) \rangle]. \quad (\text{C2})$$

Additionally, since the phase distribution can be asymmetric, we have to be careful about how we evaluate the order parameters:

$$R = \sqrt{\left[ \int \cos(\varphi(\omega)) g(\omega) d\omega \right]^2 + \left[ \int \sin(\varphi(\omega)) g(\omega) d\omega \right]^2}. \quad (\text{C3})$$

So now the self-consistency iteration has to be done for both  $S = \langle \sin(\varphi) \rangle$ ,  $S2 = \langle \sin(2\varphi) \rangle$  and  $C = \langle \cos(\varphi) \rangle$ , with

$$S = \langle \sin(\varphi) \rangle = \int \sin(\varphi) g(R[\sin(\varphi) - S] + \frac{1}{2} aR[\sin(2\varphi) - S2])(R \sin(\varphi) + aR^2 \sin(2\varphi)) d\varphi, \quad (\text{C4a})$$

$$S2 = \langle \sin(2\varphi) \rangle = \int \sin(2\varphi) g(R[\sin(\varphi) - S] + \frac{1}{2} aR[\sin(2\varphi) - S2])(R \sin(\varphi) + aR^2 \sin(2\varphi)) d\varphi, \quad (\text{C4b})$$

$$C = \langle \cos(\varphi) \rangle = \int \cos(\varphi) g(R[\sin(\varphi) - S] + \frac{1}{2} aR[\sin(2\varphi) - S2])(R \sin(\varphi) + aR^2 \sin(2\varphi)) d\varphi. \quad (\text{C4c})$$

Finally, we may then calculate

$$R = \sqrt{S^2 + C^2}. \quad (\text{C5})$$

This process is fairly complicated, and we did not see that this iterative approach converges well. One might also loop through all three values  $S, S2, C$  for every  $\sigma$ , but such a process seems computationally too expensive. For these reasons, we refrained from solving the iterative scheme for asymmetric phase distributions.

#### Appendix D: Exact analysis of periodic solutions in a simplified model

For studying stability, to see where we can expect periodic solutions, we take an even simpler system, like Duchet *et al*<sup>20</sup>:  $\kappa = \frac{1}{N} \sum \kappa_i$ :

$$\dot{\varphi}_i = \omega_i - \kappa R \sin(\varphi_i), \quad (\text{D1a})$$

$$\dot{\kappa} = \varepsilon(1 + aR^2 - \kappa). \quad (\text{D1b})$$

If we consider heterogeneous frequencies drawn from a Cauchy distribution with FWHM  $\gamma$ , we can further reduce the system to two macroscopic variables  $R$  and  $\kappa$  (the phase angle of the order parameter trivially decouples):

$$\dot{R} = R \left( -\gamma + \frac{\kappa}{2}(1 - R^2) \right), \quad (\text{D2a})$$

$$\dot{\kappa} = \varepsilon(1 + aR^2 - \kappa). \quad (\text{D2b})$$

The associated fixed point conditions are

$$R_0 = \sqrt{1 - \frac{2\gamma}{\kappa_0}}, \quad \kappa_0 = 1 + aR_0^2, \quad (\text{D3})$$

where we reject the branch with  $R_0 < 0$ . We may iteratively eliminate dependencies on  $R_0$  and  $\kappa_0$  to obtain explicit parametrizations for the fixed point solutions (+ and - correspond to stable/unstable branches),

$$R_0 = \sqrt{\frac{a - 1 \pm \sqrt{(a+1)^2 - 8a\gamma}}{2a}}, \quad (\text{D4a})$$

$$\kappa_0 = \frac{a+1}{2} \pm \sqrt{\left(\frac{a+1}{2}\right)^2 - 2a\gamma}, \quad (\text{D4b})$$

where  $R_0$  is plotted in Fig. 5. The stable branch for  $\gamma = 0$  is  $R = 1$  if  $a > -1$ , and else  $R = 1/\sqrt{|a|}$ .

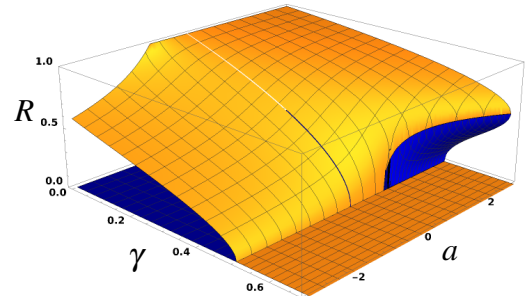


FIG. 5. Solution branches for  $R$  from the simplified Duchet-Bick model (D1).

The (linear) variational equation is  $\dot{\vec{x}} = \mathbf{J} \cdot \vec{x}$  where  $\vec{x} =$

$[\Delta R, \Delta \kappa]^T$  with  $\Delta R = R - R_0$ ,  $\Delta \kappa = \kappa - \kappa_0$  and the Jacobian

$$\mathbf{J} = \begin{bmatrix} -R_0^2 \kappa_0 & \gamma \frac{R_0}{\kappa_0} \\ 2a\epsilon R_0 & -\epsilon \end{bmatrix}. \quad (\text{D5})$$

The determinant and trace are

$$\det J = \epsilon R_0^2 \left( \kappa_0 - \frac{2\gamma}{\kappa_0} \right), \quad (\text{D6})$$

$$\text{Tr} J = -\epsilon - R_0^2 \kappa_0. \quad (\text{D7})$$

A saddle-node bifurcation between a saddle point and a stable node occurs when  $\det J = 0$  and  $\text{Tr} J < 0$ . The trace remains always negative, since we consider positive values of  $\epsilon$  and  $R_0$  only, and  $\kappa_0$  can also be shown to be positive for all parameters of concern. The determinant is positive for  $a > -1$ , and otherwise negative. To see this we only have to ask where  $\kappa_0 - \frac{2\gamma}{\kappa_0}$  changes sign. Applying the fixed point solution (D4b) to this condition, we find that crossing the  $a = -1$  boundary, the saddle-node bifurcation occurs. As a consequence, the Duchet model does not display non-stationary states above  $a = -1$  (see Discussion).

- <sup>1</sup>A. Pikovsky, M. Rosenblum, and J. Kurths, *Synchronization: A Universal Concept in Nonlinear Sciences*, Cambridge Nonlinear Science Series (Cambridge University Press, 2001).
- <sup>2</sup>S. H. Strogatz, *Sync: The Emerging Science of Spontaneous Order* (Hachette Books, 2003).
- <sup>3</sup>“Mechanisms of sinoatrial pacemaker synchronization: a new hypothesis.” *Circ. Res.* **61**, 10.1161/01.RES.61.5.704.
- <sup>4</sup>M. Rohden, A. Sorge, M. Timme, M. Timme, and D. Witthaut, “Self-organized synchronization in decentralized power grids,” **109** (2012), 10.1103/PHYSREVLETT.109.064101.
- <sup>5</sup>W. Singer and C. M. Gray, “Visual feature integration and the temporal correlation hypothesis,” **18** (1995), 10.1146/ANNUREV.NE.18.030195.003011.
- <sup>6</sup>P. J. Uhlhaas, P. J. Uhlhaas, W. Singer, and W. Singer, “Neural synchrony in brain disorders: Relevance for cognitive dysfunctions and pathophysiology,” **52** (2006), 10.1016/J.NEURON.2006.09.020.
- <sup>7</sup>P. Seliger, S. C. Young, and L. S. Tsimring, “Plasticity and learning in a network of coupled phase oscillators,” **65** (2002), 10.1103/PHYSREVE.65.041906.
- <sup>8</sup>Y. L. Maistrenko, B. Lysyansky, C. Hauptmann, O. Burylko, and P. A. Tass, “Multistability in the kuramoto model with synaptic plasticity,” *Phys. Rev. E* **75**, 066207 (2007).
- <sup>9</sup>E. A. Martens and K. Klemm, “Transitions from trees to cycles in adaptive flow networks,” *Frontiers in Physics* **5** (2017), 10.3389/fphy.2017.00062.
- <sup>10</sup>H. Mestre, T. Du, A. M. Sweeney, G. Liu, A. J. Samson, W. Peng, K. N. Mortensen, F. F. Stæger, P. A. R. Bork, L. Bashford, E. R. Toro, J. Tithof, D. H. Kelley, J. H. Thomas, P. G. Hjorth, E. A. Martens, R. I. Mehta, O. Solis, P. Blinder, D. Kleinfeld, H. Hirase, Y. Mori, and M. Nedergaard, “Cerebrospinal fluid influx drives acute ischemic tissue swelling,” *Science* **367**, eaax7171 (2020), <https://www.science.org/doi/pdf/10.1126/science.aax7171>.

- <sup>11</sup>J. P. Taylor-King, D. Basanta, S. J. Chapman, and M. A. Porter, “Mean-field approach to evolving spatial networks, with an application to osteocyte network formation,” *Phys. Rev. E* **96**, 012301 (2017).
- <sup>12</sup>B. Skyrms and R. Pemantle, “A dynamic model of social network formation,” in *Adaptive Networks: Theory, Models and Applications*, edited by T. Gross and H. Sayama (Springer Berlin Heidelberg, Berlin, Heidelberg, 2009) pp. 231–251.
- <sup>13</sup>W. Gerstner and W. M. Kistler, “Mathematical formulations of hebbian learning,” *Biol. Cybern.* **87** (2002), 10.1007/S00422-002-0353-Y.
- <sup>14</sup>B. Jüttner and E. A. Martens, “Complex dynamics in adaptive phase oscillator networks,” *Chaos: An Interdisciplinary Journal of Nonlinear Science* **33**, 053106 (2023).
- <sup>15</sup>Y. Kuramoto, “Self-entrainment of a population of coupled non-linear oscillators,” In *International Symposium on Mathematical Problems in Theoretical Physics* (1975).
- <sup>16</sup>S. H. Strogatz, “From kuramoto to crawford: exploring the onset of synchronization in populations of coupled oscillators,” *Physica D: Nonlinear Phenomena* **143**, 1–20 (2000).
- <sup>17</sup>E. A. Martens, E. Barreto, S. H. Strogatz, E. Ott, P. So, and T. M. Antonsen, “Exact results for the kuramoto model with a bimodal frequency distribution,” *Physical Review E—Statistical, Nonlinear, and Soft Matter Physics* **79**, 026204 (2009).
- <sup>18</sup>M. Thiele, R. Berner, P. A. Tass, E. Schöll, and S. Yanchuk, “Asymmetric adaptivity induces recurrent synchronization in complex networks,” *Chaos: An Interdisciplinary Journal of Nonlinear Science* **33**, 023123 (2023).
- <sup>19</sup>M. R. Sales, S. Yanchuk, and J. Kurths, “Recurrent chaotic clustering and slow chaos in adaptive networks,” (2024), arXiv:2402.17646.
- <sup>20</sup>B. Duchet, C. Bick, and Á. Byrne, “Mean-field approximations with adaptive coupling for networks with spike-timing-dependent plasticity,” **35**, 1481–1528 (2023).
- <sup>21</sup>J. Guckenheimer and P. Holmes, *Nonlinear oscillations, dynamical systems, and bifurcations of vector fields*, Vol. 42 (Springer Science & Business Media, 2013).
- <sup>22</sup>C. Kuehn *et al.*, *Multiple time scale dynamics*, Vol. 191 (Springer, 2015).
- <sup>23</sup>This is why some oscillators can drift or lock depending on initial conditions since they can adjust their coupling to either  $\kappa_i^{\text{st}} = 1$  if they are drifting or  $\kappa_i^{\text{st}} = 1 + aR \cos(\phi_i^{\text{st}})$  if they lock.
- <sup>24</sup>Note that the limit  $\epsilon \rightarrow 0$  therefore gives a lower bound of  $R$  for the general case  $\epsilon > 0$ , since in the latter the drifters have a positive net contribution.
- <sup>25</sup>Only 1 or 2 phase values for each frequency because we only consider maximal locking states (“*all that can lock, do lock*”), otherwise one technically could talk about having a distribution of phase values for frequencies that allow for locking and drifting (green strip in Fig. 2).
- <sup>26</sup>The states are stable against small perturbations of any oscillator, but in the continuum limit any perturbation to a single oscillator can be considered small to the system so we call them neutrally stable.
- <sup>27</sup>For initial conditions  $\kappa_i$  are set to a high positive value if  $|\omega_i| < \omega_{\text{thr}}$  and to a high negative value otherwise. The  $\omega_{\text{thr}} = c\sigma$  determines the size of the antipodal cluster.
- <sup>28</sup>E. Ott and T. M. Antonsen, “Low dimensional behavior of large systems of globally coupled oscillators,” *Chaos: An Interdisciplinary Journal of Nonlinear Science* **18**, 037113 (2008).
- <sup>29</sup>C. Bick, M. Goodfellow, C. R. Laing, E. A. Martens, and E. A. Martens, “Understanding the dynamics of biological and neural oscillator networks through exact mean-field reductions: a review,” *Journal of Mathematical Neuroscience* **10** (2020), 10.1186/S13408-020-00086-9.